Title

Secondary magnesite formation from forsterite under CO2 sequestration conditions via coupled heterogeneous nucleation and crystal growth

Authors

Steefel, Carl I

Yang, Li

Publication Date

2021-10-01

DOI

10.1016/j.gca.2021.07.030

Available online at www.sciencedirect.com

ScienceDirect

Geochimica et Cosmochimica Acta 311 (2021) 29–42

Geochimica et Cosmochimica Acta

www.elsevier.com/locate/gca

Secondary magnesite formation from forsterite under CO_2 sequestration conditions via coupled heterogeneous nucleation and crystal growth

Carl I. Steefel*, Li Yang

Energy Geosciences Division, Lawrence Berkeley National Laboratory, Berkeley, CA 94720, USA

Received 10 May 2021; accepted in revised form 25 July 2021; available online 2 August 2021

Abstract

Flow-only and coupled flow-diffusion experiments at 95 °C and 100 bars p_{CO2} carried out in micro-capillary tubes packed with forsterite mineral grains were used to constrain a coupled classical heterogeneous nucleation and crystal growth reactive transport model describing the formation of secondary magnesite. The study made use of a novel experimental setup in which one capillary tube for flow is connected via a three-way tee to a perpendicular capillary tube sealed at the distal end in which only molecular diffusion is allowed to occur—an experimental analogue of a single fracture-rock matrix system. While the high flux of CO_2 bearing fluids and their low pH did not result in the formation of secondary carbonates in the flow-dominated channels, as much as 2.7% magnesite formed in a diffusion-controlled capillary tube sample after 300 hours of reaction. The precipitation of secondary magnesite was not uniformly distributed, however, but showed a distinctive peak shaped pattern along the sample reacted as quantified by RAMAN spectroscopic analysis. About 50% of the total magnesite precipitation formed within a narrow interval of a few millimeters close to the middle of the 3 cm diffusion sample. To simulate the behavior of the diffusion–reaction column, and in particular the pronounced mm scale peak at approximately 1.8 cm, an interfacial free energy of approximately 70 $mJ \cdot m^{-2}$ combined with a relatively high crystal growth rate for secondary magnesite was required. In agreement with the observations based on RAMAN spectroscopy, the simulations suggest that more than 50% of Mg^{2+} dissolved from the primary forsterite precipitated as secondary magnesite. The magnesite precipitation at the central peak position in the diffusion sample showed such rapid growth that it created a local minimum in pore fluids Mg^{2+} concentration close to the peak, creating a “nucleation shadow” that focused continued growth there as nearby regions had no nucleation seeds available for crystal growth. Continued crystal growth on the initial magnesite band acted to further increase the reactive surface area at this point, thus enhancing the spatially focused crystal growth rate and creating a positive feedback leading to pattern formation. This highlights the potentially critical role of an initial nucleation event in controlling mineral precipitation patterns in subsurface porous media, patterns that may determine how the pore structure subsequently evolves physically and chemically over time due to reactive flow and transport.

Keywords: Nucleation; Crystal growth; Secondary mineral precipitation; Forsterite dissolution; Magnesite; CO_2; Reactive transport

1. INTRODUCTION

Incongruent mineral reactions that involve the dissolution of a primary phase followed by the precipitation of one or more secondary phases are key processes involved in the geochemical evolution of many subsurface systems,

---

* Corresponding author.
E-mail address: CISteefel@lbl.gov (C.I. Steefel).

https://doi.org/10.1016/j.gca.2021.07.030
0016-7037/

and includes applications related to chemical weathering, CO_2 sequestration, fluid-driven metamorphic reactions, and fracture-matrix interaction. In addition to the effects on the mineralogical and geochemical evolution of subsurface media and the resulting effects on reactivity, such reactions may play a critical role in determining the evolution of permeability and diffusivity via modifications to the pore structure. Dissolution of primary minerals tends to create porosity and permeability (Steefel and Lasaga, 1990, 1994; Elkhoury et al., 2013; Deng et al., 2016; Seigneur et al., 2019), while mineral precipitation tends to reduce permeability and diffusivity (Noiriel et al., 2012; Noiriel et al., 2016; Deng et al., 2021), and in extreme cases, to clog it completely (Steefel and Lichtner, 1994; Chagneau et al., 2015). As demonstrated by Noiriel et al. (2016), the details of nucleation and subsequent crystal growth in porous media may exert a first order control on how the physical and chemical properties of porous and fractured media evolve over time.

Modeling of irreversible incongruent reactions in the geochemical literature has been considered since at least the pioneering paper of Helgeson et al. (1969). More formal reactive transport formulations date to the seminal work of Lichtner (1985), although the first examples in which mineral precipitation affected physical transport properties (permeability, diffusivity) appear to be those of Steefel and Lasaga (1994) and Steefel and Lichtner (1994). Perhaps not readily apparent to those not immersed in the field of reactive transport modeling (RTM), however, is the fact that most analytical and numerical treatments of secondary mineral formation via incongruent geochemical reactions do not formally consider an explicit nucleation process. Key in this regard is the development and subsequent evolution of reactive surface area for the secondary minerals. In place of a formal treatment of nucleation, numerical RTMs have tended to employ ad hoc schemes in which reactive surface area for the secondary phase is either initially present as a "seed" for subsequent crystal growth, or the secondary mineral seeds magically appear at some stage in the simulation. An exception is the study of Steefel and Van Cappellen (1990), where precipitation via a classical heterogeneous nucleation model was considered to initiate the development of the secondary mineral growth. More recently, Li et al. (2017) included a newly developed classical heterogeneous nucleation formulation implemented in the RTM software CrunchTope (Steefel et al., 2015).

In this study, we consider incongruent reactions leading to secondary mineral formation in CO_2 sequestration applications. Geological CO_2 sequestration by injecting anthropogenic CO_2 into deep underground geological reservoirs for long term storage is an attractive alternative for mitigating the anthropogenic CO_2 emissions into atmosphere (Benson and Surles, 2006; Oelkers et al., 2008). The injected CO_2 can dissolve into subsurface pore fluids, a process called "solubility trapping". These CO_2 containing fluids produced can then further react with and promote the dissolution of bedrock minerals, releasing cations into pore fluids. Some of the released cations, such as Ca^{2+} and Mg^{2+}, can combine with dissolved carbonate species and form secondary carbonates precipitates. This process permanently traps the CO_2 injected underground by converting them into solid thermodynamically stable minerals, a process called "mineral trapping" (Benson et al., 2003; Benson and Surles, 2006). In order to quantitatively understand those processes and make defensible and rigorous predictions of the long terms fate and stability of the injected CO_2 underground, it is critical to have a thorough understanding of the kinetic reactions between bedrock minerals and CO_2 bearing fluids in subsurface porous medium. Although a number of studies have been carried out to study the kinetics of mineral fluids reactions relevant to geological CO_2 sequestration conditions, most of these were focused on mineral dissolution reactions conducted in batch reactors (Giammar et al., 2005; Saldi et al., 2013). Only a few studies have been devoted to understanding the kinetics of secondary carbonate precipitation during CO_2 injection (e.g., (Li et al., 2017; Noiriel et al., 2016). Moreover, most of the experimental studies were performed in conventional batch reactors where it was not possible to consider subsurface porous medium effects (Hänchen et al., 2008). It is very challenging to apply the baseline kinetic information obtained in well-stirred batch reactors to predict mineral carbonation reactions in subsurface porous media environments where minerals are in contact with reactive fluids within tiny pores of a few to a hundred microns in diameter characterized by very different solid/solution ratios and hydrodynamic flow conditions. Following a separate track, many studies focused on the transport and reactions associated with CO_2 injection under advective flow-controlled regimes (Andreani et al., 2009). However, except for the initial transient period during CO_2 injection, most of the injected CO_2 is expected to be trapped inside geological formations as a relatively stagnant (non-mobile) phase where diffusion may be the dominant transport mechanism. This is particularly true for the length of time required to form secondary carbonate precipitates.

Subsurface porous medium is generally characterized by varying degree of heterogeneity. During CO_2 injection, the high permeability zones are expected to be filled quickly with CO_2 bearing fluids. However, this may not be the case for low permeability zones where the dissolved CO_2 content in the pore fluids rises only gradually through diffusion dominant processes. Such diffusion-controlled regimes are likely to play an important role during the long-term storage of geological CO_2 underground, yet relatively few studies have been devoted to understanding the effect of diffusion processes on the formation of secondary carbonates. In this study, kinetic experiments were conducted using high temperature and pressure micro-capillary tube reactors so as to investigate the coupled dissolution and secondary mineral precipitation during reactions of olivine (forsterite) with CO_2 bearing fluids in simulated microporous environment. A novel micro-capillary tube reactor was designed to study the coupled mineral dissolution and secondary carbonates precipitation in flow or diffusion dominant regimes separately. To describe quantitatively the behavior of the reactive system under diffusion-controlled conditions, a coupled heterogeneous nucleation and crystal growth model for secondary magnesite formation was developed.

2. EXPERIMENTAL MATERIALS AND METHODS

A novel micro-capillary tube reactor was designed to study the coupled mineral dissolution and secondary carbonates precipitation under both flow and diffusion-dominant regimes respectively. Fused silica micro-capillary tubing (200 μm I.D. 360 μm O.D.) was cut into different lengths and packed with forsterite mineral grains to simulate reactions taking place in subsurface micro-porous environments. Such micro-capillary tube reactors are able to withstand pressures up to 200 bars and temperatures over 200 C. The thin walls of the micro-capillary tubing are fabricated with pure fused silica, which is transparent to RAMAN signals and allows for analysis of the solid samples after reactions by RAMAN spectroscopy without significant sample disturbance. The very small dimensions of the capillary tube samples allow for a complete scan of the entire solid samples after reaction, thus providing detailed information on the occurrence and distribution of potential secondary minerals.

The illustration of the experimental system setup is shown in Fig. 1. Forsterite minerals used in the experiment are almost pure natural forsterite grains purchased from Wards Scientific. Electron Microprobe analysis of the forsterite grains indicated they were 92% Fo with a chemical composition of $(Mg_{1.84}Fe_{0.16})SiO_4$. First, a forsterite rock specimen was gently crushed, with removal of any impurities under the microscope. The forsterite grains singled out were further crushed and sieved to a particle size of 45 to 53 μm. The sieved forsterite mineral grains were washed free of fine particles with D. I. water and dried in an oven at 60 °C before their use in the experiment.

The forsterite grains obtained above were then packed into the fused silica micro-capillary tube of 3 cm length and secured in place from both ends by two 2 cm long plugs made of empty fused silica capillary tube (185 μm O.D. and 50 μm I.D). The masses of empty micro-capillary tubes and plugs were weighed before and after packing to obtain the net mass of forsterite particles packed inside. The total volume of the micro-capillary tube packed with forsterite grains and the total mass of the packed forsterite particles were used to calculate the porosity of the grain pack. The dry, sieved forsterite particles were also measured for their specific surface area by multipoint BET analysis using an Autosorb-1 surface area analyzer. Several sets of forsterite grains packed with identical micro-capillary tubes were prepared for experimental use, with two sets used to conduct flow only and coupled diffusion-flow scenarios.

Since the precipitation of secondary minerals was directly driven by primary minerals dissolution in these experiments (i.e., there was no supersaturation with respect to secondary phases at the micro-capillary tube inlet), it is necessary to first understand the dissolution kinetics of primary forsterite minerals. For this purpose, a 6 cm long forsterite-packed capillary tube sample was reacted with CO_2 bearing fluids at a 0.01 $\mu L \cdot min^{-1}$ flow rate at 95 °C and 100 bars pressures to study its reaction kinetics. This value of the flow rate was chosen so as to result in a measurable change in concentration in the capillary tube. This single experiment constituted the “flow-only” experiment

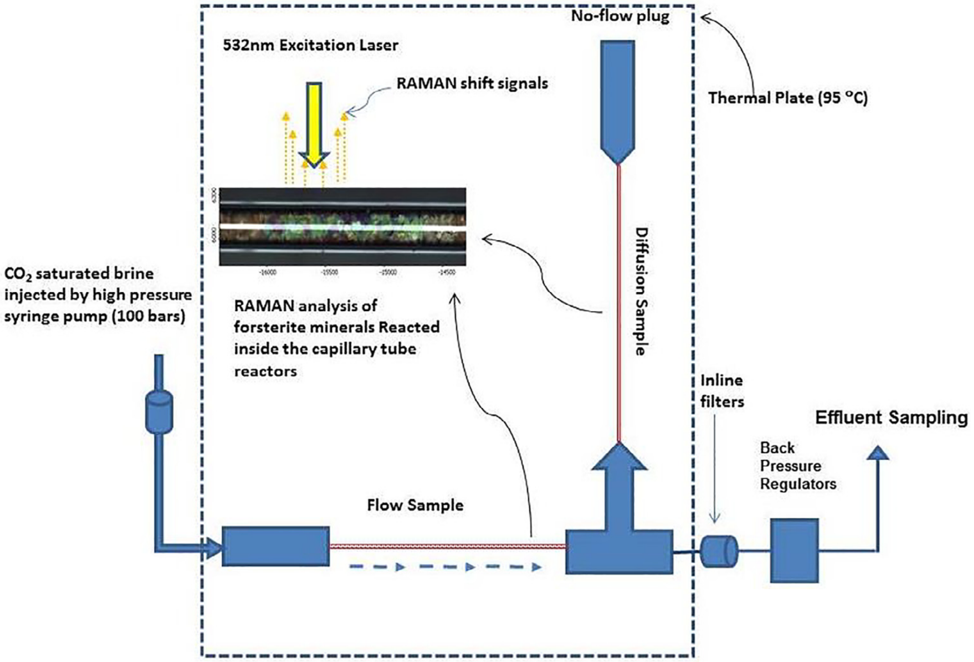

Fig. 1. Illustration of the capillary tube experiment setup for the diffusion and flow coupled experiments and RAMAN analysis on the samples reacted. Flow occurs from left to right in the tube marked “Flow Sample” past the tee, through the back-pressure regulator, and on to effluent sampling. Diffusion is in a perpendicular capillary tube (marked “Diffusion Sample”) connected via a 3-way micro-tee to the flow capillary tube. This diffusion-only tube has a no-flow plug at the end. Only the diffusion-controlled portion was simulated with reactive transport modeling.

referred to in Table 1, and was used as the basis for estimating the rate of forsterite dissolution. For the diffusion-flow coupled experiment discussed in Table 2, two forsterite packed capillary tube samples were used, one of 6 cm for flow and the other 3 cm in length for diffusion. The 6 cm long forsterite packed capillary tube sample was used as the flow channel directly connected to the ISCO high pressure syringe pump charged with CO_2 bearing fluid. The other 3 cm long capillary tube sample was used as the coupled diffusion sample with its one end connected to the downstream end of the flow sample at right angles through a 3-way micro-tee connector. The distal end of the coupled diffusion sample was sealed with a PEEK micro-union plug, thus forming effectively a no flux boundary. A higher flow rate in the flow channel was used in the diffusion-flow experiment so as to maintain constant concentration conditions at the juncture of the diffusion-controlled tube (i.e., effectively a Dirichlet boundary condition). Detailed information on the experimental samples and conditions described above are listed in Table 1.

The flow-only experiment was not modeled, but was used to determine the rates of forsterite dissolution as a function of the pH and pCO_2 conditions. The diffusion–reaction modeling discussed below focused on the diffusion-controlled experiment, since this is the only one where magnesite formation was observed.

Before the experiment was begun, both flow-only and diffusion coupled flow samples as well as the entire assembled experimental device were thoroughly flushed with 0.01 M NaCl solution to saturate the system with background electrolyte fluids and to remove any air bubbles inside. To complete the experimental setup, the assembled samples were further connected to a 0.5 micron inline filter and a back pressure regulator (preset at 100 bars pressure) through micro-unions and 1/32″ O.D. PEEK tubing. The effluent passing through the experiment system was collected into plastic vials that were periodically sampled for ICP-MS analysis to represent effluent chemistry from the reactor. The stock CO_2 bearing solution used in the experiment study has a CO_2/H_2O mole ratio of 1:90, a value slightly lower than the maximum dissolvable CO_2 calculated according to the equation of state proposed by Duan and Sun (2003) and Duan et al. (2006) at given experiment temperature, pressure and fluid salinity. Such a value was chosen to make sure that all of the CO_2 was dissolved and to avoid the uncertainties of reactions with a supercritical phase. To prepare the stock CO_2 bearing fluids, specified amounts of pure CO_2 gas and 0.01 M NaCl solution were drawn into a high pressure ISCO syringe pump first, after which all pump valves were closed so that the pressurized mixed gas and solution system resulted in complete dissolution of all of the CO_2 gas at the given pressure.

The CO_2 bearing fluids prepared in this fashion were then injected into the experimental system according to the specified flow rates using the high pressure ISCO syringe pump described above. Throughout the course of the experiment, the entire system was placed on top of a constant temperature hotplate calibrated and preset at 95 °C. The assembled experimental devices were further covered with aluminum alloy covers to keep them at a uniform constant temperature during the experimental run. After the experiment, the entire experimental apparatus was carefully disassembled and the reacted samples (forsterite + precipitate) were mounted on glass microscope slides on a

Table 1
Samples information and conditions in the experimental study.

	Flow only experiment	Diffusion-flow coupled experiment	
Sample type	Advective flow sample	Advective flow controlled sample	Diffusion controlled sample
Forsterite packed capillary tube sample length (cm)	6	6	3
Sample porosity	0.57	0.55	0.5
Flow rate (µL/min)	0.01	0.09	N.A.
Injection stock solution	CO_2/H_2O of 1:90 in 0.01 M NaCl, TIC: 620 mmol/L		
Experiment temperature (°C)	95	95	
Experiment pressure (bars)	100	100	
Experiment duration (hours)	256	300	

Table 2
Parameters used in diffusion–reaction modeling of forsterite-magnesite capillary tube diffusion experiment.

Parameter	Units	Value
Forsterite rate constant	$mol \cdot m^{-2} \cdot s^{-1}$	3.75×10^{-8}
Magnesite interfacial free energy	$mJ \cdot m^{-2}$	70
Pre-exponential (A_0J_0)	$nuclei \cdot m^{-3} \cdot s^{-1}$	1000
Specific surface area of nucleating magnesite	$m^2 \cdot g^{-1}$	500
Forsterite surface area	$m^2 \cdot g^{-1}$	0.08
Magnesite rate constant	$mol \cdot m^{-2} \cdot s^{-1}$	1.0×10^{-5}
Magnesite molar volume	$cm^3 \cdot mol^{-1}$	28.08

RAMAN instrument for solid phase analysis. RAMAN analysis was performed on a Thermo-Fisher RAMAN microscope with a 10 mW, 532 nm laser. To quantify the amount of magnesite formed in the experiment sample, crushed pure magnesite mineral grains and the forsterite particles used in the experiment were mixed together at known ratios and packed into the same experiment capillary tube so as to provide an external calibration standard. Those mixture standards were scanned by RAMAN spectroscopy mapping under the same analysis conditions as the reacted samples. The integrated signals obtained were then used to construct the calibration curve for quantifying secondary magnesite formed in the experimental sample.

3. EXPERIMENTAL RESULTS

The forsterite-packed capillary tube sample in the flow-only experiment was reacted with CO_2 bearing stock fluids at 95 °C and 100 bars for approximately 250 hours, while the diffusion and flow coupled experiment samples were reacted for 300 hours. At the conclusion of the experiments, both samples were disassembled for solid phase characterization by RAMAN spectroscopy analysis. The solution chemistry of effluent samples collected during the experiment run was analyzed by ICP-MS and is shown in Fig. 2. In the single flow-only forsterite dissolution experiment that was carried out, effluent Mg and Si showed roughly stoichiometric dissolution during the course of the experiment.

3.1. Forsterite dissolution rate

The average effluent Mg and Si concentrations from forsterite dissolution in the flow only experiments were used to obtain and refine kinetic rate expressions for the dissolution of forsterite minerals used in this experiment study. The effect of CO_2 on forsterite dissolution was very similar to the effects observed in pH catalyzed reactions as the reacting fluids were acidified by dissolved CO_2 under pressure. Based on the study by Hänchen et al. (2006), a general Transition State Theory (TST) rate law of forsterite dissolution can be expressed as $r = k\exp(-E_aRT)$, in which k is the dissolution rate constant ranging from 94 to 7554 mol m^{-2} s^{-1} depending on the specific samples used, the activation energy $E_a = 60.2$ kJ mol^{-1} k^{-1} for reactions above 90 °C, and the pH dependence rate parameter $n = 0.46 \pm 0.03$. Two sets of effluent chemistry data from dissolution of forsterite samples under very different flow rate scenarios were used to refine rate parameters that best described the dissolution kinetics of the forsterite samples used in the experiments. One was from the flow only experiment running at 0.01 μL min^{-1} flow rate and the other from the diffusion coupled flow experiment sample running at 0.09 μL min^{-1} flow rate. Using the activation energy of 60.2 kJ and a temperature of 95 °C, it was found that a pH dependence parameter n of 0.48 and a rate constant of 3.75×10^{-8} mol m^{-2} s^{-1} provided the best fit to the forsterite dissolution behavior at 95 °C observed under both experimental conditions (Fig. 2). The overall dissolution rate expression for the forsterite sample used in this study at given experiment conditions can be summarized as:

$$r\ (\mathrm{mol}\cdot \mathrm{m}^{-2}\cdot \mathrm{s}^{-1}) = 3.75\times 10^{-8} a_{H+}^{0.48} \qquad (1)$$

This rate equation was used to model dissolution of the forsterite sample in the diffusion-controlled capillary tube experiment reactor as a basis for investigating the coupled secondary carbonate precipitation process.

3.2. RAMAN analysis

Solid sample analysis by RAMAN spectroscopy indicated that for the forsterite packed micro-capillary sample under advective flow-controlled regime (hereafter referred to as the ‘flow sample’), there were no detectable secondary carbonates formed in the reacted sample. Very minor amounts of secondary iron oxide formation as a grain coating developed as a result of the release of iron from primary forsterite minerals. In contrast, significant amounts of secondary carbonate were identified by RAMAN spectroscopic analysis in the forsterite packed capillary tube sample carried out under the diffusion-controlled regime (hereafter referred to as the ‘diffusion sample’). The mineral

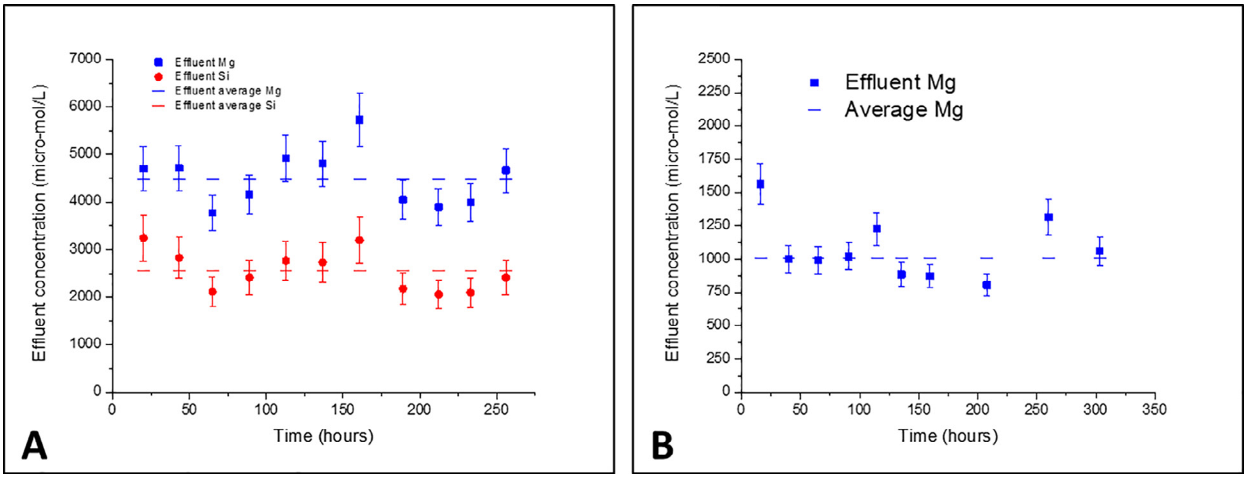

Fig. 2. Effluent solution chemistry of (A) the flow only and (B) the coupled diffusion-flow experiments.

magnesite was identified as the only secondary carbonate to form (Fig. 3).

The RAMAN analysis also indicated that secondary magnesite was not uniformly distributed over the extent of the diffusion-controlled portion of the micro-capillary tube, but showed instead a distinctive pattern with a peak at about 18.5 mm from the inlet end of the forsterite grain pack (Fig. 4). The amount of secondary magnesite precipi-

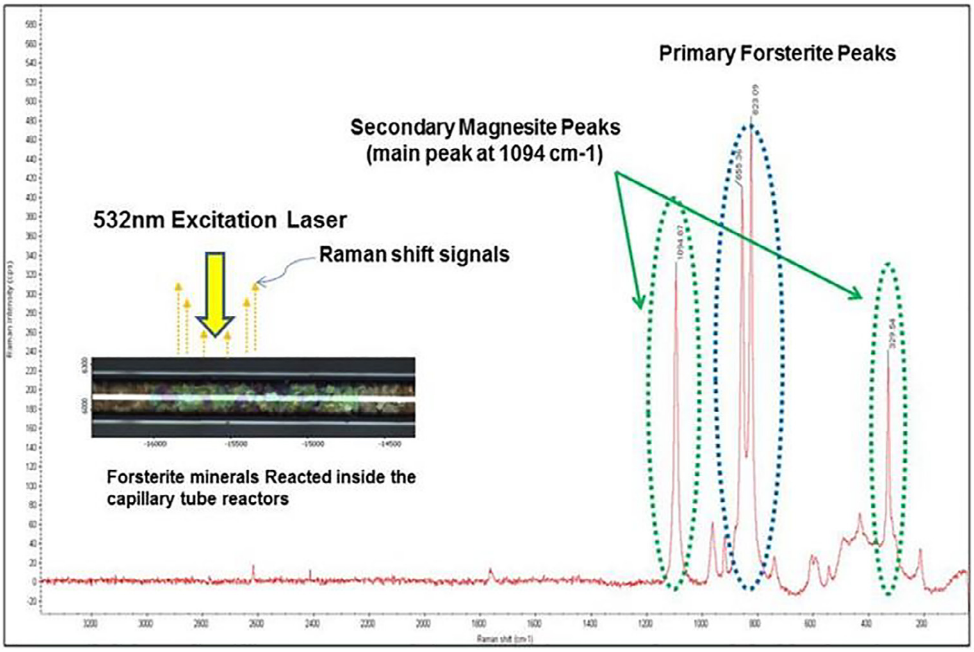

Fig. 3. RAMAN spectrum of secondary magnesite formed in the diffusion sample about 1.8 cm from the 3-way tee connector to the flow tube.

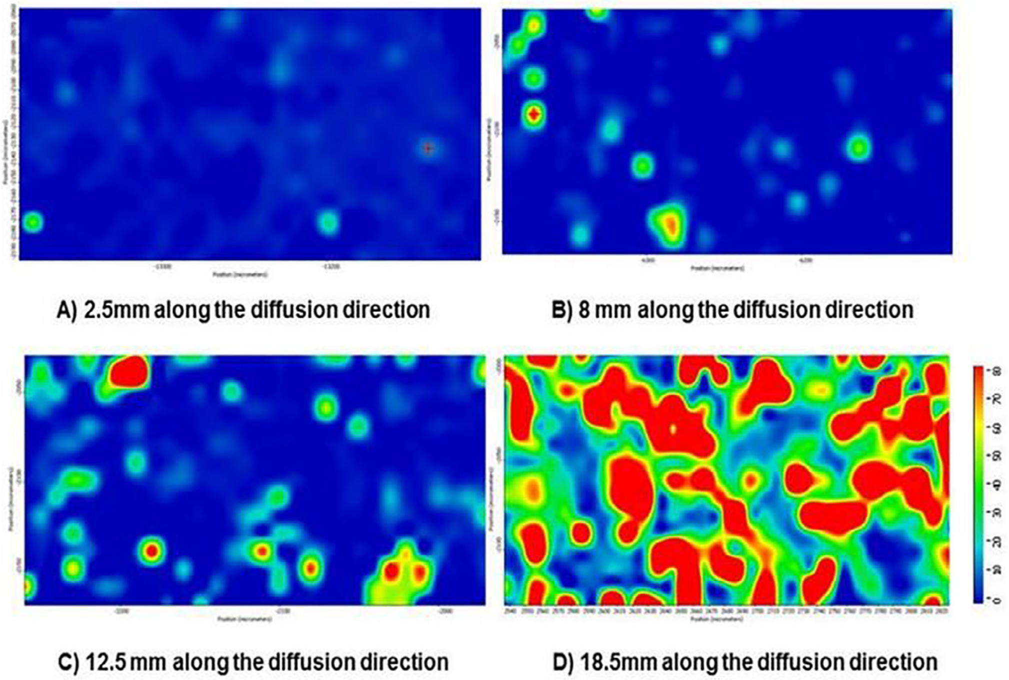
A) 2.5mm along the diffusion direction

B) 8 mm along the diffusion direction

C) 12.5 mm along the diffusion direction

D) 18.5mm along the diffusion direction

Fig. 4. Secondary magnesite formed in the diffusion sample by RAMAN spectroscopic mapping scan (a warmer color indicates higher intensities from magnesite 1094 cm^{-1} peak).

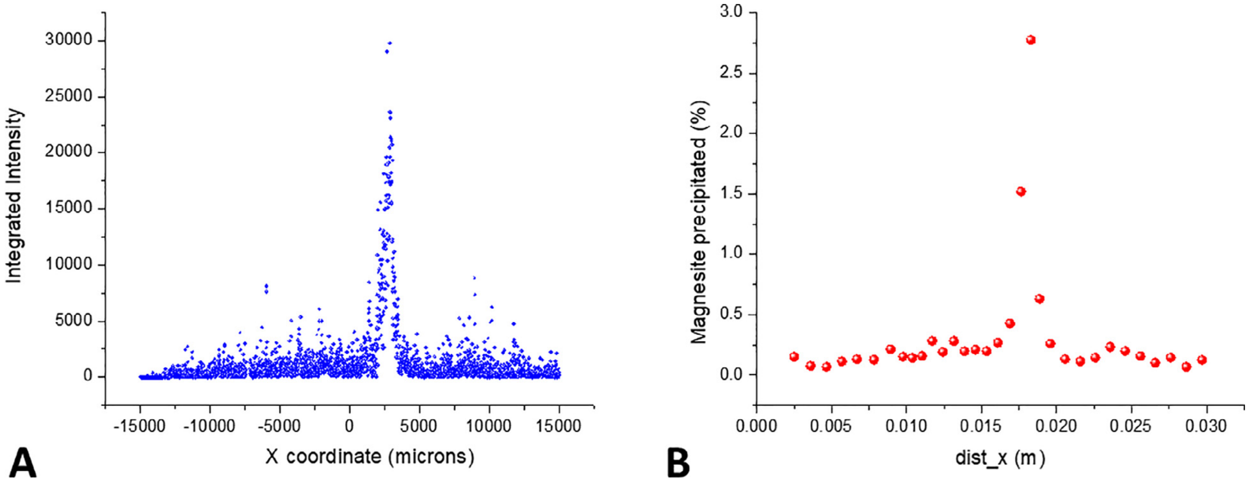

Fig. 5. (A) Integrated intensities of secondary magnesite peaks (the 1094 cm^{-1} Raman peak) along the diffusion sample and (B) Corresponding magnesite precipitation profile based on calibration with external standards.

tation formed was quantified by carrying out a scan of the reacted sample with RAMAN spectroscopy for all secondary magnesite precipitated, then integrating the intensities of magnesite according to its characteristic RAMAN peak at 1094 cm^{-1} at given areas along the reacted sample, and then comparing those integrated intensities with an external calibration curve. It was found that small peaks of magnesite occur within a few millimeters of the inlet side of the diffusion sample, but generally at only low concentrations of about 0.2% at most. Further into the diffusion sample (moving away from the CO_2-charged flow channel), there was a sharp increase in the amount of magnesite precipitated close to the middle of the diffusion sample, reaching as much as 2.7%. Beyond that peak, the intensities of secondary magnesite peaks decreased markedly to much lower values of about 0.2% over the rest of the diffusion sample (Fig. 5). Most magnesite particles were of a few microns in size and indicated significant growth from initial tiny magnesite nuclei (Fig. 6).

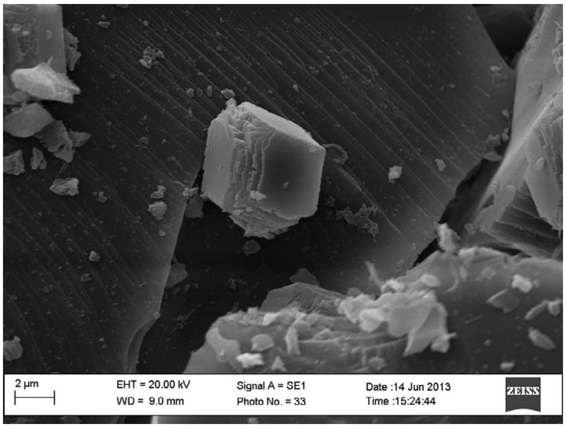

Fig. 6. Secondary magnesite formed in diffusion sample on forsterite grains.

4. MODELING APPROACH FOR COUPLED HETEROGENEOUS NUCLEATION AND CRYSTAL GROWTH

In this section, we develop a general model for coupled heterogeneous nucleation and crystal growth, with the additional objective of using this to describe quantitatively the results from Raman spectroscopy presented above. This capability is important for many reactive transport applications in particular (Steefel and Van Cappellen, 1990; Noiriel et al., 2016; Li et al., 2017; Prasianakis et al., 2017; Deng et al., 2021). It is perhaps not widely recognized that most of the widely available numerical reactive transport software does not include explicit capabilities for mineral nucleation, whether homogeneous or heterogeneous (Steefel et al, 2015). The need for some such treatment is clear by examining a general form of a rate, R_m, for heterogeneous mineral growth or dissolution (see Steefel and Van Cappellen, 1990; Steefel and Lasaga, 1994; Steefel et al., 2015), presented here as following a Transition State Theory (or TST) form (although the same conclusion would be drawn for any mineral rate law, TST or not):

$$R_m = A_m k_m \left(\prod a^n\right)\left|\left(Q_m K_{eq}\right)^{\eta} - 1\right|^m \mathrm{sign}\left[\ln Q_m K_{eq}\right] \qquad (2)$$

where A_m is the surface area ($m^2\ m^{-3}$) of the growing or dissolving phase, k_m is the rate constant (mol $m^{-2}\ s^{-1}$), $(\prod a^n)$ is the product of catalytic and inhibitory effects (e.g., pH), $Q_m K_{eq}$ is the ion activity product divided by the equilibrium constant for the reaction, "*sign*" refers to the sign of the expression that follows, and η and m are experimentally determined exponents for the dependence on the free energy of reaction (or the supersaturation). The problem in neglecting nucleation is that the value for the surface area in Eq. (2) must be then chosen in an ad hoc fashion, typically with some guess as to a "seed" secondary mineral concentration and grain size. If a secondary phase is not initially present via a seed and nucleation is neglected, then of course the rate for growth remains always zero. This need to include a seed secondary mineral (distributed where?) can be circumvented by including a formal mineral nucleation expression, which can be thought of as an additional pathway within the overall mineral growth reaction network. Typically, nucleation occurs in advance of crystal growth, but this is not required and depends on the local conditions determining the rates of the individual nucleation versus crystal growth pathways.

Although there has been considerable discussion of nucleation mechanisms and their corresponding mathematical representation recently, for the purposes of this study it is sufficient to make use of a classical heterogeneous nucleation expression (De Yoreo and Vekilov, 2003), particularly since the experimental data cannot readily discriminate between the different mechanisms. The rate of nucleation for the secondary phase, J_n (number of nuclei per volume per time, or nuclei m^{-3} s^{-1}) can be written as (Steefel and Van Cappellen, 1990; De Yoreo and Vekilov, 2003; Li and Jun, 2018; Devos et al., 2021):

$$J_n = J_0 \exp\left[\frac{-\Delta g_n}{k_B T}\right] \tag{3}$$

where Δg_n is the Gibbs free energy of the critical nucleus, J_0 is the pre-exponential factor, k_B is Boltzmann's constant, and T is the absolute temperature. The Gibbs free energy for the critical nucleus is defined by:

$$\Delta g_n = 163\pi\sigma^3\left[\frac{\upsilon}{k_B T \ln QK_{eq}}\right]^2 \tag{4}$$

where σ is the interfacial free energy (mJ m^{-2}), υ is the molecular volume (m^3), and ln(Q/Keq) is the logarithm of the supersaturation. From Eq. (4), it is evident that Δg_n depends on the cube of the interfacial free energy in the numerator and the square of the supersaturation, that is:

$$\Delta g_n \propto \frac{\sigma^3}{(\ln QK_{eq})^2} \tag{5}$$

The nucleation rate converted to a molar rate (mol s^{-1}) is then given by

$$R_{nucleation} = A_0 J_0 \exp\left[-\frac{16\pi\upsilon^2}{3k_B^3 T^3}\frac{\sigma^3}{(\ln QK_{eq})^2}\right]A_{template} \tag{6}$$

where J_0 has units of nuclei m^{-3} s^{-1}, $A_{template}$ is the surface area (m^2 m^{-3}) of the template available for nucleation, and A_0 (mol m $nuclei^{-1}$) provides conversion to units of the mineral rate (mol m^{-3} s^{-1}). A rigorous conversion factor from nuclei per unit time to aqueous concentrations requires additional assumptions about nucleus geometry, but these are not explored here (see Li and Jun, 2018).

Homogeneous nucleation can be treated with a similar expression if the surface area of the templating phase is dropped and the interfacial free energy and pre-exponential term are adjusted as needed. In this study we focus on heterogeneous nucleation because the assumption is that it is energetically more favorable than homogeneous nucleation. Alternatively, we could have included both pathways, with a higher interfacial free energy for the homogeneous nucleation pathway, but since substrate (forsterite) is available everywhere in the diffusion cell, it is not expected that this would have changed the results presented here. As with any heterogeneous nucleation expression, the behavior is largely governed by the ratio of the interfacial free energy to the supersaturation of the solution with respect to the secondary phase, as is apparent from the proportionality given in Eq. (5). Larger values of the interfacial free energy require correspondingly higher supersaturations to achieve observable nucleation (Steefel and Van Cappellen, 1990).

Note that no inhibitory or catalytic effects are explicitly considered in the treatment of nucleation represented in Eq. (6). This is primarily due to the fact that we considered only a single background electrolyte consisting of NaCl, thus there is no data available from this study to evaluate this effect. However, this is not a limitation of the model presented here, which can readily incorporate inhibitory and/or catalytic effects on the nucleation rate.

In this study, the surface area of the template is that of forsterite, which is the dissolving phase releasing Mg^{2+} into solution that increases the supersaturation with respect to the secondary phase magnesite. Thus, the overall precipitation rate for magnesite, $R_{ppt\text{-}magn}$ (mol m^{-3}), including both nucleation and crystal growth pathways is given by:

$$\begin{aligned} R_{ppt-magn} = {} & \underbrace{A_0 J_0 \exp\left[-\frac{16\pi\upsilon^2}{3k_B^3 T^3}\frac{\sigma^3}{(\ln QK_{eq})^2}\right]A_{forst}}_{\text{Nucleation}} \\ & + \underbrace{A_{magn} k_{magn}\left[Q_{magn} K_{eq_{magn}} - 1\right]}_{\text{Crystal Growth}} \end{aligned} \tag{7}$$

where we have adopted a simpler linear form of the TST rate law, and where the *magn* and *forst* subscripts refer to the parameters for magnesite and forsterite, respectively. In the modeling, this precipitation reaction is combined with the dissolution reaction for forsterite, which follows the expression in Eq. (1) to simulate the overall rate-limited geochemical evolution of the system. Here, one can think of the first term on the right-hand side of Eq. (7) (the nucleation pathway) as providing the surface area, A_{magn}, for magnesite crystal growth (the second term on the right-hand-side). Eventually the surface area for crystal growth increases sufficiently to the point where the crystal growth pathway becomes the dominant mechanism (Steefel and Van Cappellen, 1990). As discussed further below, the nucleation event itself may not generate large amounts of reactive surface area, but this stage of the coupled precipitation process determines at least the location of the initial seed that develops further via crystal growth. This observation again is very important for understanding the subsequent evolution of the physical pore structure (affecting transport properties via the permeability and effective diffusivity) and reactivity.

Depending on the rate of crystal growth relative to the transport rate (here molecular diffusion), the crystal growth pathway can decrease the local supersaturation, thus suppressing continued nucleation within a "shadow zone" on either side. As discussed below, this effect is most prominent where the nucleation barrier resulting from the interfacial free energy is high and crystal growth is sufficiently rapid that the solution supersaturation is decreased below some

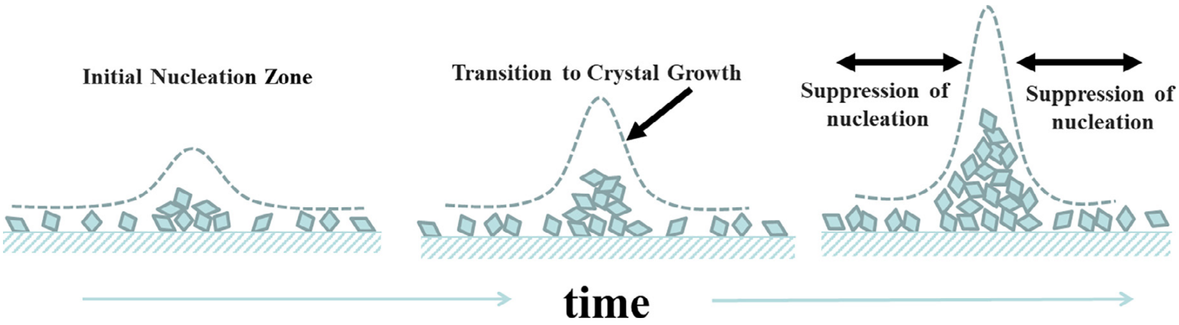

Fig. 7. Conceptual model for the formation of a nucleation peak. Initial nucleation is followed by a transition to crystal growth once the surface area of the secondary phase increases sufficiently. Crystal growth at the location of the initial nucleation zone then creates a "shadow zone" within which nucleation is suppressed due to the lowering of the supersaturation of the secondary phase within some diffusion distance of the peak.

threshold value determined by the interfacial free energy for the relevant phase (see Fig. 4 in Steefel and Van Cappellen, 1990). The combination of a distinct nucleation zone (corresponding eventually to a peak in the secondary mineral concentration) and a "nucleation shadow zone" can lead to pattern formation, as discussed in the literature (Ortoleva et al., 1987; Jamtveit and Meakin, 1999; Jamtveit and Hammer, 2012). For this case, the conceptual model is as shown in Fig. 7, with the formation of an initial nucleation zone followed by a gradual transition to crystal growth (the surface area term for magnesite increasing to the point where crystal growth becomes rapid at this location), followed by the development of the "shadow zone" where the growth decreases the supersaturation within some diffusion distance of the nucleation peak.

Table 3
Boundary and initial conditions for coupled heterogeneous nucleation and crystal growth simulations.

Chemical Component	Left Boundary Condition	Initial Condition
pH	3.23	7.51
p_{CO2}	100 bars	0.01 bars
Units in μmol·kgw^{-1}		
Na^+	10,000.00	10,000.00
Cl^-	10,000.00	10,000.00
Mg^{2+}	0.01	950.00
$SiO_2(aq)$	0.01	100.00

5. REACTIVE TRANSPORT MODELING OF CAPILLARY TUBE EXPERIMENT

5.1. Model setup

To set up the reactive transport simulation, the forsterite packed sample (3 cm in length) within the capillary tube is discretized with 100 grid cells of 0.3 mm each. Since the left side of the capillary tube is connected to a perpendicular capillary tube down which the high pCO$_2$ fluid is flowing (100 bars pCO$_2$, see Fig. 1), it is treated as a Dirichlet (or fixed concentration) boundary condition (Table 1 and Table 3). The flow past the tee marking the beginning of the diffusion cell is sufficiently rapid that the concentration is maintained effectively at a constant value. The right-hand side is sealed (Fig. 1 and Fig. 8), and is thus treated as a no-flux boundary condition. The mass of forsterite sample in each grid cell of the diffusion reactor was calculated assuming a homogeneous distribution of the total mass of forsterite inside the capillary tube.

The diffusion from the high pCO$_2$ solution flowing through the perpendicular capillary tube results in the dissolution of the forsterite, with a rate law best represented by Eq. (1). The release of Mg^{2+} into solution and the con-

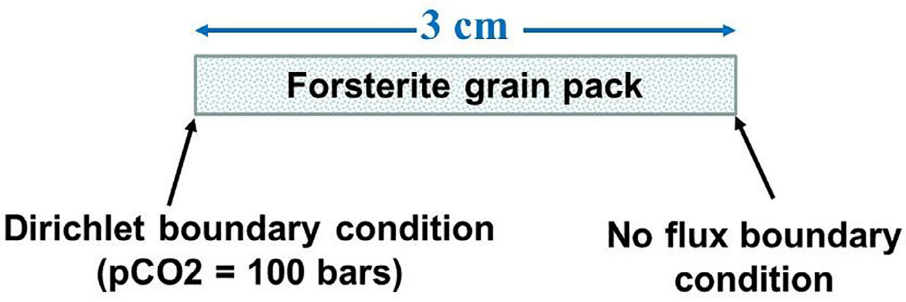

Fig. 8. Schematic of diffusion–reaction modeling domain (diffusion-only capillary tube). The Dirichlet or fixed boundary condition on the left-hand side is created by the fast flow of CO$_2$-charged fluid along the flow capillary tube (see Fig. 1).

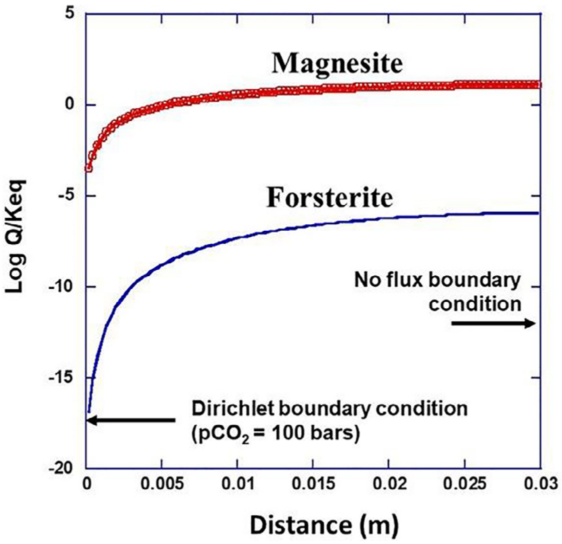

Fig. 9. Simulated magnesite and forsterite saturation states (Log Q/K_{eq}) in the capillary tube as a result of *forsterite dissolution only* (no magnesite precipitation).

sumption of hydrogen ion according to the reaction stoichiometry:

$$Mg_2SiO_4 + 4H^+ \rightarrow 2Mg^{2+} + SiO_2(aq) \quad (8)$$

results in the supersaturation of the solution in the capillary tube with respect to magnesite $MgCO_3(s)$, which will precipitate according to the reaction:

$$Mg^{2+} + CO_2(aq) \rightarrow MgCO_3(s) + 2H^+ \quad (9)$$

assuming CO_2 (aq) is the dominant species (at pH values above the pK_{a1}, bicarbonate will be the relevant dominant species). The simulated profile of the magnesite and forsterite saturation state as a result of *forsterite dissolution only* (no magnesite precipitation) is shown in Fig. 9. Supersaturation with respect to magnesite develops approximately ½ way down the length of the tube from the left.

In the simulations magnesite is assumed to precipitate according to the combined nucleation and crystal growth rate law given in Eq. (7). It should be noted again that magnesite cannot form via crystal growth until sufficient surface area has been generated by the nucleation step. Where the magnesite nucleates depends on where the supersaturation rises sufficiently that the nucleation rate is non-negligible, i.e., the nucleation threshold is surpassed. The increase in the magnesite supersaturation requires that the forsterite dissolution rate be sufficiently fast relative to the diffusion rate in the capillary that the Mg^{2+} and pH rise sufficiently, but also that magnesite crystal growth does not locally consume Mg^{2+} and produce H^+ such that the supersaturation falls below the critical threshold value that results from the highly nonlinear form of the nucleation rate law given in Eq. (6). Where the latter effect occurs, a "nucleation shadow" can develop, as in Fig. 7.

5.2. Modeling results

The simulations provide a good match with the magnesite weight percent from the Raman spectroscopy if an interfacial free energy of 70 mJ·m^{-2} is combined with a rate constant of 10^{-5} mol · m^2 · s^{-1} for magnesite crystal growth via the TST formulation given in Eq. (7) (Fig. 10) and used together with the diffusion coefficients in Table 4.

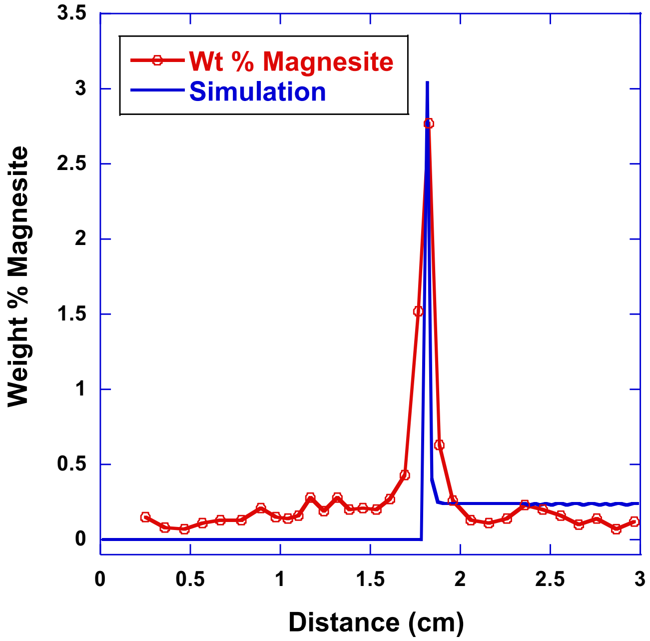

Fig. 10. Best match of Raman spectroscopy-derived data for magnesite weight percent with CrunchTope simulation using an interfacial free energy of 70 mJ·m^{-2} and a rate constant of 10^{-5} mol · m^2 · s^{-1} for magnesite crystal growth based on values given in Table 1. High p_{CO2} (100 bars) is on left side of capillary tube (at X = 0), while the right-hand side is plugged (no flux). Transport consists of only molecular diffusion as described by the Nernst-Planck equation.

Table 4
Self-diffusion coefficients for chemical species considered in simulations. Molecular diffusion is calculated using the Nernst-Planck equation (see Steefel et al, 2015).

Chemical component	Diffusion coefficient $\left(m^2 \cdot s^{-1}\right)$
H+	9.00×10^{-9}
$CO_2(aq)$	1.60×10^{-9}
Na^+	1.30×10^{-9}
Cl^-	2.10×10^{-9}
Mg^{2+}	0.65×10^{-9}
$SiO_2(aq)$	1.00×10^{-9}
OH^-	4.50×10^{-9}

The magnesite "shoulder" between 0.25 and 1.75 cm was not possible to capture with the modeling because, as is evident from Fig. 9, supersaturation initially occurs with respect to magnesite at about this distance from the high pCO_2 boundary on the left. At distances between the peak and the Dirichlet boundary condition at $X = 0$, the lack of supersaturation in the idealized homogeneous 1D model system precludes magnesite formation. However, it may be that grain scale heterogeneity in the experimental system results in local supersaturation between 0 and about 1.75 cm and this could account for the magnesite observed in this region. Alternatively, there may have been some movement of the magnesite precipitates into the portion of the tube between 0 and 1.75 cm, although every effort was made to avoid the development of pressure gradients that might cause this.

The time evolution of the system out to 150 hours is shown in Fig. 11. Before 50 hours, no secondary magnesite forms at all, after which the peaks and shoulders amplify in proportion to their height. Note the intensification of the local peaks as compared to the "shoulder" or plateau region between 1.8 and 3.0 cm, a reflection of the positive feedback between increasing reactive surface area and the reactivity. This is in fact the primary explanation for the formation of the peak, which after the initial nucleation event (relatively short lived), is dominated by the crystal growth mechanism that accelerates as the reactive surface area increases locally at the site of the peak. Faster magnesite growth produces more reactive surface area, which then enhances the local accumulation at the expense of nearby regions. Coarsening of the magnesite (which does occur, as is evident from Fig. 5) would tend to reduce the rate of increase of the magnesite reactive surface area, but this effect is not included in the modeling (it was considered in Steefel and Van Cappellen, 1990). In this modeling, the assumption is that the total reactive surface area per grid cell is determined by the total mass of magnesite multiplied by the specific surface area (assumed to be a constant 500 $m^2 \cdot g^{-1}$ in the simulations, see Table 2). Thus, the rate of increase of the magnesite surface area via crystal growth is linear with respect to the mass precipitated.

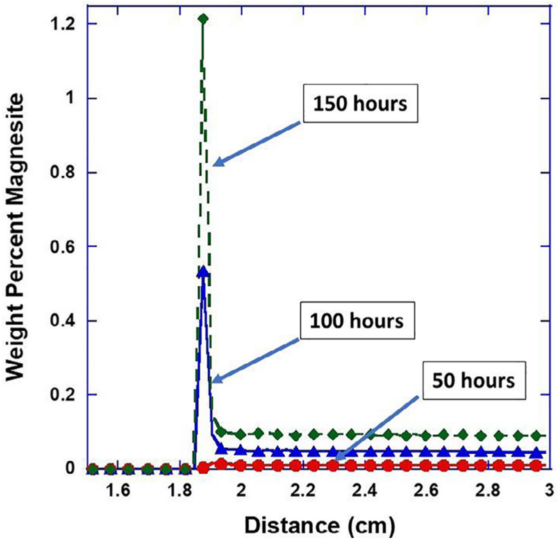

Fig. 11. Time evolution of the secondary magnesite weight percent between 50 and 150 hours. Prior to 50 hours, magnesite does not form at all due to lack of supersaturation.

The effect of different parameters, of which the most important are the interfacial free energy and the magnesite crystal growth rate, is more complicated than the time evolution alone. Lowering the interfacial free energy has the effect of migrating the secondary magnesite peak to the left, closer to the high pCO_2 boundary, as a result of the lower supersaturation threshold (see curve in Fig. 12A for 45 $mJ \cdot m^{-2}$). Interfacial free energy values for calcite nucleating on quartz range from 36-48 $mJ \cdot m^{-2}$ depending on the salinity of the solution (Li and Jun, 2018) to as much as 97 $mJ \cdot m^{-2}$ ((Van Cappellen, 1991). No values have been reported for magnesite. Higher values of the interfacial free energy (95 and 120 $mJ \cdot m^{-2}$) produce additional peaks in the magnesite distribution—presumably the base case value of 70 $mJ \cdot m^{-2}$ would produce a similar if a larger experimental domain (>3 cm) was considered. The effect of the value chosen for the magnesite crystal growth rate is also significant (Fig. 11B), since it affects both the rate of amplification of the magnesite profiles and the extent of sharpening of the peaks. Perhaps non-intuitively, a growth rate of $10^{-5} mol \cdot m^{-2} \cdot s^{-1}$ produces the largest magnesite peak, but this is in part because the additional peaks that develop at higher rates (10^{-4}) result in partitioning the available Mg^{2+} released from forsterite dissolution into multiple peaks.

6. DISCUSSION

The reactive transport modeling of the capillary tube incorporating coupled heterogeneous nucleation and crystal growth mechanisms emphasize the complexity of incongruent geochemical systems, of which the conversion of forsterite to magnesite under high pCO_2 conditions is just an example. Nucleation determines the position and the early rate of magnesite formation and surface area evolution, while subsequent crystal growth (which becomes significant only after the seed nuclei are formed) determines the rate of amplification of the profile, but also the sharpness of the peaks as result of the positive feedback between crystal growth and reactivity via reactive surface area evolution. While the heterogeneous nucleation step produces the initial peak shaped distribution of magnesite seeds onto

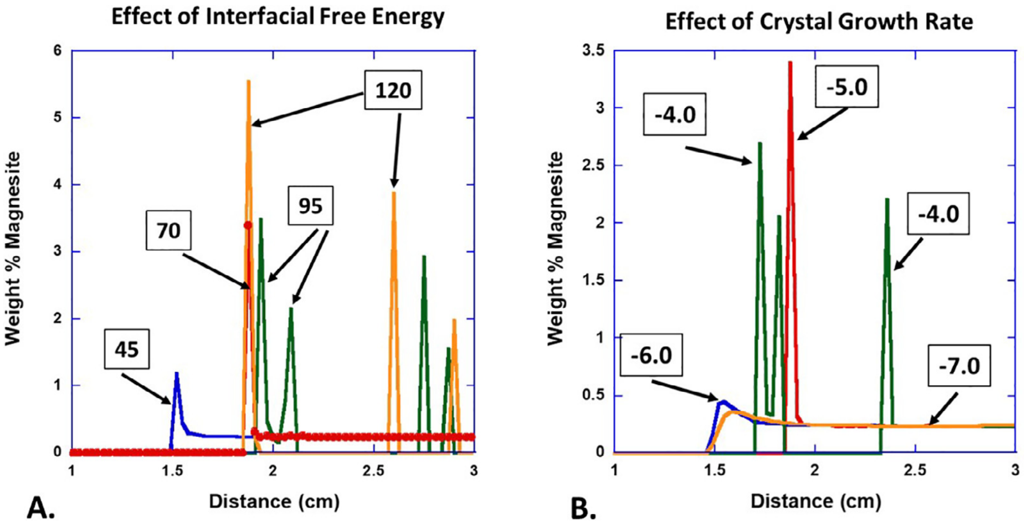

Fig. 12. (A) Effect of interfacial free energy on distribution of secondary magnesite at 300 hours assuming a magnesite crystal growth rate of 10^{-5}mol · m^{-2} · s^{-1}. (B). Effect of the magnesite crystal growth rate (log values shown) at 300 hours using a base case value of 70 mJ·m^{-2} for the magnesite interfacial free energy.

primary forsterite surfaces, the nucleation process alone cannot account for the full development of the pattern. The development of the peaks and resulting pattern has to rely on the continuing growth step to maintain and further enhance the initial peak shaped distribution of magnesite precipitation that developed as a result of the initial heterogeneous nucleation event. This is an observation from the modeling that the nucleation event is relatively short-lived, and not involving a significant portion of the total mass of magnesite formed. It is also confirmed from the SEM images of the secondary magnesite formed in the diffusion sample, which show that continued growth from nanometer scale nuclei to crystals up to 5 μm in size occurred. The modeling and the observations both emphasize that reactive surface area evolution during the crystal growth stage is required to explain the precipitation pattern.

The rate of diffusive transport also impacts the behavior by determining the first appearance of magnesite supersaturation (faster diffusion pushes this threshold to the right, away from the high $p\mathrm{CO}_2$ boundary), but also the width of the nucleation “shadow” bordering the secondary mineral peaks. This implies that uncertainties in the diffusion rate, whether due to the intrinsic diffusion coefficients, or in real geological media as a result of tortuosity effects, will affect the results.

In this study, a classical one step heterogeneous nucleation model was used. This was primarily because this is the simplest approach to describing the data—the available data do not allow for the development of a more complex non-classical or multi-step model. To develop a more sophisticated and comprehensive model would require both additional temporal and spatial resolution, even down to the scales of individual crystallites (e.g., (Jun et al., 2010; Li and Jun, 2019). In this regard, the classical heterogeneous nucleation model is not suggested as universally applicable to all incongruent reactions.

As we have discussed, the novel experimental setup shown in Fig. 1 provides a first order representation of a fracture-rock matrix system. In a real system, however, not all of the minerals may be in contact with the pore fluid through which diffusion is occurring. This effect could reduce the availability of a substrate for nucleation, but also potentially reduce the dissolution rate of the primary phase. Dead-end pores, that is those that are not connected to the macroporosity, would contribute less to the overall system reactivity. Lacking an experimental study on a real sediment or sedimentary rock, however, it is not useful to speculate on how important these effects are, but the studies of Beckingham et al. (2016, 2017) suggest that these effects could be quite important.

7. CONCLUSIONS

In this study, we have used the conversion of forsterite to magnesite under high $p\mathrm{CO}_2$ conditions as an example of an incongruent reaction in which coupled heterogeneous nucleation and crystal growth control the spatial distribution and the evolving reactivity of the geochemical system. The model development and application are based on novel capillary tube experiments that show that secondary carbonate formation, while thermodynamically inhibited in the main flow channel due to the low pH, can still occur in local micro-environments characterized by diffusion-controlled transport conditions. This highlights the importance of local heterogeneities in controlling minerals carbonation reactions in the subsurface during geological carbon sequestration. Within the diffusion–reaction cell, magnesite formed in significant amounts only with a relatively narrow peak approximately halfway down the tube. The diffusion–reaction modeling predicts that the generation of nuclei from an initial nucleation event transitions relatively quickly to crystal growth, resulting in the development of a positive feedback as reactive surface area generation increases the local precipitation rate. We have demonstrated this behavior for a CO_2 injection system, but the results are much more general and are expected to appear in other systems where incongruent geochemical reactions are important. These include chemical weathering, metamorphic mineral reactions, and fracture-matrix in subsurface systems. While based on a classical one-step heterogeneous model, the analysis could be relatively easily extended to more complex nucleation rate laws if additional data were available.

Declaration of Competing Interest

The authors declare that they have no known competing financial interests or personal relationships that could have appeared to influence the work reported in this paper.

ACKNOWLEDGMENTS

This work was supported as part of the Center for Nanoscale Control of Geologic CO_2, an Energy Frontier Research Center funded by the U.S. Department of Energy, Office of Science, Basic Energy Sciences. Additional support was provided by the Director, Office of Science, Basic Energy Sciences, Chemical Sciences, Geosciences, and Biosciences Division, of the U.S. Department of Energy as part of funding to the Fundamental Geoscience program. Both funding streams are under Contract No. DE-AC02-05CH11231 to Lawrence Berkeley National Laboratory.

RESEARCH DATA PACKAGE AND OPEN SOURCE CODE AVAILABILITY

The research data for this study are available from a DRYAD data repository: Steefel, Carl; Yang, Li (2021), *Secondary Magnesite Formation under CO2 Sequestration Conditions via Coupled Heterogeneous Nucleation and Crystal Growth*, Dryad, Dataset, https://doi.org/10.7941/D1P35S. The source code for CrunchTope used to run the simulations can be found at: github.com/CISteefel/CrunchTope.

REFERENCES

Andreani M., Luquot L., Gouze P., Godard M., Hoise E. and Gibert B. (2009) Experimental study of carbon sequestration reactions controlled by the percolation of CO_2-rich brine through peridotites. *Environ. Sci. Technol.* **43**, 1226–1231.

Beckingham L. E., Mitnick E. H., Steefel C. I., Zhang S., Voltolini M., Swift A. M., Yang L., Cole D. R., Sheets J. M. and Ajo-Franklin J. B. (2016) Evaluation of mineral reactive surface area estimates for prediction of reactivity of a multi-mineral sediment. *Geochim. Cosmochim. Acta* **188**, 310–329.

Beckingham L. E., Steefel C. I., Swift A. M., Voltolini M., Yang L., Anovitz L. M., Sheets J. M., Cole D. R., Kneafsey T. J. and Mitnick E. H. (2017) Evaluation of accessible mineral surface areas for improved prediction of mineral reaction rates in porous media. *Geochim. Cosmochim. Acta* **205**, 31–49.

Benson S. M., Apps J., Hepple R., Lippmann M., Tsang C. F. and Lewis C. (2003) Health, safety and environmental risk assessment for geologic storage of carbon dixide: Lessons learned from industrial and natural analogues. In *Greenhouse Gas Control Technologies-6th International Conference*. Elsevier, pp. 243–248.

Benson S. M. and Surles T. (2006) Carbon dioxide capture and storage: An overview with emphasis on capture and storage in deep geological formations. *Proc. IEEE* **94**, 1795–1805.

Chagneau A., Tournassat C., Steefel C. I., Bourg I. C., Gaboreau S. P., Esteve I. N., Kupcik T., Claret F. and Schäfer T. (2015) Complete restriction of 36Cl–diffusion by celestite precipitation in densely compacted illite. *Environ. Sci. Technol. Lett.* **2**, 139–143.

De Yoreo J. J. and Vekilov P. G. (2003) Principles of crystal nucleation and growth. *Rev. Mineral. Geochem.* **54**, 57–93.

Deng H., Molins S., Steefel C., DePaolo D., Voltolini M., Yang L. and Ajo-Franklin J. (2016) A 2.5 D reactive transport model for fracture alteration simulation. *Environ. Sci. Technol.* **50**, 7564–7571.

Deng H., Tournassat C., Molins S., Claret F. and Steefel C. (2021) A pore-scale investigation of mineral precipitation driven diffusivity change at the column-scale. *Water Resour. Res.*, e2020WR028483.

Devos C., Van Gerven T. and Kuhn S. (2021) A review of experimental methods for nucleation rate determination in large-volume batch and microfluidic crystallization. *Cryst. Growth Des.* **21**, 2541–2565.

Duan Z. and Sun R. (2003) An improved model calculating CO_2 solubility in pure water and aqueous NaCl solutions from 273 to 533 K and from 0 to 2000 bar. *Chem. Geol.* **193**, 257–271.

Duan Z., Sun R., Zhu C. and Chou I.-M. (2006) An improved model for the calculation of CO_2 solubility in aqueous solutions containing Na^+, K^+, Ca^{2+}, Mg^{2+}, Cl^-, and SO_4^{2-}. *Mar. Chem.* **98**, 131–139.

Elkhoury J. E., Ameli P. and Detwiler R. L. (2013) Dissolution and deformation in fractured carbonates caused by flow of CO_2-rich brine under reservoir conditions. *Int. J. Greenhouse Gas Control* **16**, S203–S215.

Giammar D. E., Bruant, Jr., R. G. and Peters C. A. (2005) Forsterite dissolution and magnesite precipitation at conditions relevant for deep saline aquifer storage and sequestration of carbon dioxide. *Chem. Geol.* **217**, 257–276.

Hänchen M., Prigiobbe V., Baciocchi R. and Mazzotti M. (2008) Precipitation in the Mg-carbonate system—effects of temperature and CO_2 pressure. *Chem. Eng. Sci.* **63**, 1012–1028.

Hänchen M., Prigiobbe V., Storti G., Seward T. M. and Mazzotti M. (2006) Dissolution kinetics of fosteritic olivine at 90–150 C including effects of the presence of CO_2. *Geochim. Cosmochim. Acta* **70**, 4403–4416.

Helgeson H. C., Garrels R. M. and MacKenzie F. T. (1969) Evaluation of irreversible reactions in geochemical processes involving minerals and aqueous solutions—II. Applications. *Geochim. Cosmochim. Acta* **33**, 455–481.

Jamtveit B. and Hammer Ø. (2012) Sculpting of rocks by reactive fluids. *Geochem. Perspect.* **1**, 341–342.

Jamtveit B. and Meakin P. (1999) Growth, dissolution and pattern formation in geosystems. In *Growth, Dissolution and Pattern Formation in Geosystems*. Springer, pp. 1–19.

Jun Y.-S., Lee B. and Waychunas G. A. (2010) In situ observations of nanoparticle early development kinetics at mineral–water interfaces. *Environ. Sci. Technol.* **44**, 8182–8189.

Li Q. and Jun Y.-S. (2018) The apparent activation energy and pre-exponential kinetic factor for heterogeneous calcium carbonate nucleation on quartz. *Commun. Chem.* **1**, 1–9.

Li Q. and Jun Y.-S. (2019) Salinity-induced reduction of interfacial energies and kinetic factors during calcium carbonate nucleation on quartz. *J. Phys. Chem. C* **123**, 14319–14326.

Li Q., Steefel C. I. and Jun Y.-S. (2017) Incorporating nanoscale effects into a continuum-scale reactive transport model for CO_2-deteriorated cement. *Environ. Sci. Technol.* **51**, 10861–10871.

Lichtner P. C. (1985) Continuum model for simultaneous chemical reactions and mass transport in hydrothermal systems. *Geochim. Cosmochim. Acta* **49**, 779–800.

Noiriel C., Steefel C. I., Yang L. and Ajo-Franklin J. (2012) Upscaling calcium carbonate precipitation rates from pore to continuum scale. *Chem. Geol.* **318**, 60–74.

Noiriel C., Steefel C. I., Yang L. and Bernard D. (2016) Effects of pore-scale precipitation on permeability and flow. *Adv. Water Resour.* **95**, 125–137.

Oelkers E. H., Gislason S. R. and Matter J. (2008) Mineral carbonation of CO_2. *Elements* **4**, 333–337.

Ortoleva P., Merino E., Moore C. and Chadam J. (1987) Geochemical self-organization I; reaction-transport feedbacks and modeling approach. *Am. J. Sci.* **287**, 979–1007.

Prasianakis N. I., Curti E., Kosakowski G., Poonoosamy J. and Churakov S. V. (2017) Deciphering pore-level precipitation mechanisms. *Sci. Rep.* **7**, 13765.

Saldi G. D., Daval D., Morvan G. and Knauss K. G. (2013) The role of Fe and redox conditions in olivine carbonation rates: An experimental study of the rate limiting reactions at 90 and 150 C in open and closed systems. *Geochim. Cosmochim. Acta* **118**, 157–183.

Seigneur N., Mayer K. U. and Steefel C. I. (2019) Reactive transport in evolving porous media. *Rev. Mineral. Geochem.* **85**, 197–238.

Steefel C., Appelo C., Arora B., Jacques D., Kalbacher T., Kolditz O., Lagneau V., Lichtner P., Mayer K. U. and Meeussen J. (2015) Reactive transport codes for subsurface environmental simulation. *Comput. Geosci.* **19**, 445–478.

Steefel C. I. and Lasaga A. C. (1990) *Evolution of Dissolution Patterns: Permeability Change Due to Coupled Flow and Reaction*. ACS Publications.

Steefel C. I. and Lasaga A. C. (1994) A coupled model for transport of multiple chemical species and kinetic precipitation/dissolution reactions with application to reactive flow in single phase hydrothermal systems. *Am. J. Sci.* **294**, 529–592.

Steefel C. I. and Lichtner P. C. (1994) Diffusion and reaction in rock matrix bordering a hyperalkaline fluid-filled fracture. *Geochim. Cosmochim. Acta* **58**, 3595–3612.

Steefel C. I. and Van Cappellen P. (1990) A new kinetic approach to modeling water-rock interaction: The role of nucleation, precursors, and Ostwald ripening. *Geochim. Cosmochim. Acta* **54**, 2657–2677.

Van Cappellen P. S. (1991) *The Formation of Marine Apatite: A Kinetic Study*. Yale University.

Associate editor: Chen Zhu